Acta Oceanol. Sin., 2021, Vol. 40, No. 7, P. 31–41
https://doi.org/10.1007/s13131-021-1771-9
http://www.aosocean.com
E-mail: ocean2@hyxb.org.cn

The mechanism of the banded structure of drifting macroalgae in the Yellow Sea

Yan Li[1], Fangli Qiao[1, 2, 3*], Hongyu Ma[1, 2], Qiuli Shao[4], Zhixin Zhang[1], Guansuo Wang[1, 2]

[1] First Institute of Oceanography, Ministry of Natural Resources, Qingdao 266061, China

[2] Key Laboratory of Marine Sciences and Numerical Modeling, Ministry of Natural Resources, Qingdao 266061, China

[3] Laboratory for Regional Oceanography and Numerical Modeling, Pilot National Laboratory for Marine Science and Technology (Qingdao), Qingdao 266037, China

[4] Institute of Oceanographic Instrumentation, Shandong Academy of Sciences, Qilu University of Technology (Shandong Academy of Sciences), Qingdao 266100, China

Received 14 September 2020; accepted 4 November 2020

Abstract

At the end of May 2008, a massive bloom of macroalgae occurred in the western Yellow Sea off China and lasted for nearly two months, and annual blooms have occurred since then on. During bloom period, the surface-drifting macroalgae have showed an interesting pattern dominated by a banded structure, and the distance between neighboring bands ranged from hundreds of meters to about 6 km with a peak at 1–1.5 km, which is an order of higher than the scale of Langmuir circulation of 50–100 m. In order to explain this new phenomenon, ocean current data obtained from a Doppler current profiler off Qingdao was used to implement stability analysis. By numerically solving the resulting differential Orr-Sommerfeld equation, the secondary circulation induced from the instability of the Emkan current was found to fit well with the observed spatial scale of the surface-drifting macroalgae's banded structure. As the wind driven Emkan current exist universally in the global ocean, it is reasonable to conclude that the banded structure with kilometers distance between adjoining bands is ubiquitous. We found a new circulation in the upper ocean which is important for exchange of energy, materials and gas between the upper ocean and subsurface layer.

Key words: banded structure, stability analysis, secondary circulation

Citation: Li Yan, Qiao Fangli, Ma Hongyu, Shao Qiuli, Zhang Zhixin, Wang Guansuo. 2021. The mechanism of the banded structure of drifting macroalgae in the Yellow Sea. Acta Oceanologica Sinica, 40(7): 31–41, doi: 10.1007/s13131-021-1771-9

1 Introduction

In summer 2008, a massive bloom of non-toxic green macroalgae occurred in the coastal waters of the Yellow Sea off Qingdao, the host city of the 2008 Olympic Games sailing competition. And the blooms have happened annually since then on. Most of the drifting macroalgae appeared in linear bands on the sea surface. The lengths of the individual bands ranged from hundreds of meters to tens of kilometers, while the distance between the neighboring bands was about 1 km, ranging from 0.5 km to 6.0 km (Qiao et al., 2009). The water depth at the regions where algal bands appeared is about 30 m. Details about the drifting macroalgae are shown in Fig. 1.

Irving Langmuir first noticed the banded structure of floating material on the ocean surface while crossing the North Atlantic in 1927; he described how floating material was drawn into lines of convergence between pairs of vortices aligned downwind (Langmuir, 1938). This phenomenon was named as Langmuir circulation. Langmuir reported that the distance between the bands of floating Sargassum was 100–200 m, while the windrows in Lake George in his follow-up experiment had a separation of 5–25 m. Subsequent researches such as Pollard (1977), Leibovich (1983), and Thorpe (2004) reported scales ranging from 2 m to a few hundred meters. It is amzing to notice that the distance between neighboring macroalgae bands is 0.5–6.0 km, which is far greater than what is expected in Langmuir circulation, the spatial scale is about one order than that of Langmuir circulation. After the corresponding author of this paper, Fangli Qiao, published the observation results (Qiao et al., 2009), Thorpe (2009) immediately noticed the results and suggested that particles floating on the sea surface are drawn into bands by the converging flows between neighboring Langmuir cells, and the floating bands, in particular, the buoyant algae, can subsequently amalgamate as a result of Langmuir turbulence. He developed an idealized model to describe the rearrangement and dispersion of the floating particles. Although Thorpe (2009) proposed the above model, Fangli Qiao has been thinking that the banded structure should be a novel dynamic process.

Dong (1997) investigated the formation mechanism of tidal sand ridges with neighboring ridges ranging from 1 km to 10 km. That scale is on the same order as the observed spatial scale of the algal band in the Yellow Sea. Dong (1997) suggested that the sand ridges may be caused by the instability of the vertical shear of the tidal currents. However, the vertical shear of tidal current is so weak in the upper ocean, so the banded structure should be irrelevant with the instability of tidal current.

In atmospheric sciences, bands of clouds, known as "cloud

Foundation item: The National Natural Science Foundation of China under contract No. 41821004; the National Program on Global Change and Air-Sea Interaction under contract No. GASI-IPOVAI-05.
*Corresponding author, E-mail: qiaofl@fio.org.cn

streets", are also common phenomenon and have been dynamically investigated. The banded structure of cloud streets can be clearly seen in Fig. 2. Lilly (1966) explained cloud streets and enriched the theory of the atmospheric boundary layer. He suggested that cloud streets were caused by instability of the atmospheric boundary layer. Brown (1970) considered the effect of temperature stratification and concluded that the characteristic depth of eddies in the atmospheric and oceanic boundary layer is 5–7 times of the Ekman characteristic length, and the associated wavelength is 4π times of this parameter.

In order to reveal dynamic mechanism of the banded structure from the surface-drifting macroalgae on the sea surface in the Yellow Sea, we implemented the classical linear stability analysis which has been used in Dong (1997) to explain the tidal sand ridges, Lilly (1966) and Brown (1970) to explain the cloud street. We dynamically explained this interesting phenomenon based on stability analysis of the ocean currents in the surface layer. The ocean current is separated into the primary (or mean) flow and the secondary flow (disturbance). The lateral and vertical structure of the disturbance, as determined from the lateral wave-length and the vertical amplitude and phase relations, is determined by the most unstable perturbation of the solution to the first-order stability equation. The mean flow used in this paper is a set of observed ocean current profiles. Since vertical shear of mean flow is the driving force of the secondary flow, so we removed the tidal current which has no or quite weak vertical shear at the surface layer. By numerically solving the Orr-Sommerfeld equation, we obtained the growth rate of unstable perturbations for different wave numbers and deflection angles from the mean flow. The most unstable perturbation is regarded as the dynamical process responsible for the banded structure. It is amazing that the spatial scale of the most unstable perturbation fits well with that of macroalgea bands, that is, about 1 km.

2 Model

2.1 *Governing equations*

The governing equations comprise the equations of motion for a viscous, incompressible fluid in a rotating coordinate system and the continuity equations are as follows:

$$\begin{cases} \dfrac{\partial u}{\partial x}+\dfrac{\partial v}{\partial y}+\dfrac{\partial w}{\partial z}=0, \\ \dfrac{\partial u}{\partial t}+u\dfrac{\partial u}{\partial x}+v\dfrac{\partial u}{\partial y}+w\dfrac{\partial u}{\partial z}-fv=-\dfrac{1}{\rho}\dfrac{\partial p}{\partial x}+ \\ \quad A_{\mathrm{H}}\left(\dfrac{\partial^2 u}{\partial x^2}+\dfrac{\partial^2 u}{\partial y^2}\right)+A_{\mathrm{V}}\dfrac{\partial^2 u}{\partial z^2}\dfrac{\partial v}{\partial y}, \\ \dfrac{\partial v}{\partial t}+u\dfrac{\partial v}{\partial x}+v\dfrac{\partial v}{\partial y}+w\dfrac{\partial v}{\partial z}+fu=-\dfrac{1}{\rho}\dfrac{\partial p}{\partial y}+ \\ \quad A_{\mathrm{H}}\left(\dfrac{\partial^2 v}{\partial x^2}+\dfrac{\partial^2 v}{\partial y^2}\right)+A_{\mathrm{V}}\dfrac{\partial^2 v}{\partial z^2}, \\ \dfrac{\partial w}{\partial t}+u\dfrac{\partial w}{\partial x}+v\dfrac{\partial w}{\partial y}+w\dfrac{\partial w}{\partial z}=-\dfrac{1}{\rho}\dfrac{\partial p}{\partial z}-g+ \\ \quad A_{\mathrm{H}}\left(\dfrac{\partial^2 w}{\partial x^2}+\dfrac{\partial^2 w}{\partial y^2}\right)+A_{\mathrm{V}}\dfrac{\partial^2 w}{\partial z^2}, \end{cases} \tag{1}$$

where u and v are the horizontal velocity components in the x and y directions, respectively; w is the vertical velocity in the z direction; f is the Coriolis parameter; and A_{H} and A_{V} are the horizontal and vertical eddy viscosity coefficients, respectively, as other stability analysis, they are assumed to be constants.

The boundary conditions are

$$\begin{cases} u=v=w=0, \quad z=-H; \\ \dfrac{\partial u}{\partial z}=\dfrac{\partial v}{\partial z}=0, \quad w=0, \quad z=0; \end{cases} \tag{2}$$

where H is the water depth. To obtain the perturbation equations, we divide u, v, w, p into two parts, the mean and the perturbation:

$$\begin{cases} u=\overline{u}+u^*, \\ v=\overline{v}+v^*, \\ w=\overline{w}+w^*, \\ p=\overline{p}+p^*. \end{cases} \tag{3}$$

Upon substituting Eq. (3) into Eq. (1), we get the full equations:

$$\begin{cases} \left(\dfrac{\partial \overline{u}}{\partial x}+\dfrac{\partial \overline{v}}{\partial y}+\dfrac{\partial \overline{w}}{\partial z}\right)+\left(\dfrac{\partial u^*}{\partial x}+\dfrac{\partial v^*}{\partial y}+\dfrac{\partial w^*}{\partial z}\right)=0, \\ \left(\dfrac{\partial \overline{u}}{\partial t}+\dfrac{\partial u^*}{\partial t}\right)+\left(\overline{u}\dfrac{\partial \overline{u}}{\partial x}+\overline{u}\dfrac{\partial u^*}{\partial x}+u^*\dfrac{\partial \overline{u}}{\partial x}+u^*\dfrac{\partial u^*}{\partial x}\right)+ \\ \quad \left(\overline{v}\dfrac{\partial \overline{u}}{\partial y}+\overline{v}\dfrac{\partial u^*}{\partial y}+v^*\dfrac{\partial \overline{u}}{\partial y}+v^*\dfrac{\partial u^*}{\partial y}\right)+ \\ \quad \left(\overline{w}\dfrac{\partial \overline{u}}{\partial z}+\overline{w}\dfrac{\partial u^*}{\partial z}+w^*\dfrac{\partial \overline{u}}{\partial z}+w^*\dfrac{\partial u^*}{\partial z}\right)-f\overline{v}-fv^* \\ \quad =-\dfrac{1}{\rho}\dfrac{\partial \overline{p}}{\partial x}-\dfrac{1}{\rho}\dfrac{\partial p^*}{\partial x}+A_{\mathrm{H}}\left(\dfrac{\partial^2 \overline{u}}{\partial x^2}+\dfrac{\partial^2 \overline{u}}{\partial y^2}\right)+A_{\mathrm{V}}\dfrac{\partial^2 \overline{u}}{\partial z^2}+ \\ \quad A_{\mathrm{H}}\left(\dfrac{\partial^2 u^*}{\partial x^2}+\dfrac{\partial^2 u^*}{\partial y^2}\right)+A_{\mathrm{V}}\dfrac{\partial^2 u^*}{\partial z^2}, \\ \left(\dfrac{\partial \overline{v}}{\partial t}+\dfrac{\partial v^*}{\partial t}\right)+\left(\overline{u}\dfrac{\partial \overline{v}}{\partial x}+\overline{u}\dfrac{\partial v^*}{\partial x}+u^*\dfrac{\partial \overline{v}}{\partial x}+u^*\dfrac{\partial v^*}{\partial x}\right)+ \\ \quad \left(\overline{v}\dfrac{\partial \overline{v}}{\partial y}+\overline{v}\dfrac{\partial v^*}{\partial y}+v^*\dfrac{\partial \overline{v}}{\partial y}+v^*\dfrac{\partial v^*}{\partial y}\right)+ \\ \quad \left(\overline{w}\dfrac{\partial \overline{v}}{\partial z}+\overline{w}\dfrac{\partial v^*}{\partial z}+w^*\dfrac{\partial \overline{v}}{\partial z}+w^*\dfrac{\partial v^*}{\partial z}\right)+f\overline{u}+fu^* \\ \quad =-\dfrac{1}{\rho}\dfrac{\partial \overline{p}}{\partial x}-\dfrac{1}{\rho}\dfrac{\partial p^*}{\partial x}+A_{\mathrm{H}}\left(\dfrac{\partial^2 \overline{v}}{\partial x^2}+\dfrac{\partial^2 \overline{v}}{\partial y^2}\right)+A_{\mathrm{V}}\dfrac{\partial^2 \overline{v}}{\partial z^2}+ \\ \quad A_{\mathrm{H}}\left(\dfrac{\partial^2 v^*}{\partial x^2}+\dfrac{\partial^2 v^*}{\partial y^2}\right)+A_{\mathrm{V}}\dfrac{\partial^2 v^*}{\partial z^2}, \\ \left(\dfrac{\partial \overline{w}}{\partial t}+\dfrac{\partial w^*}{\partial t}\right)+\left(\overline{u}\dfrac{\partial \overline{w}}{\partial x}+\overline{u}\dfrac{\partial w^*}{\partial x}+u^*\dfrac{\partial \overline{w}}{\partial x}+u^*\dfrac{\partial w^*}{\partial x}\right)+ \\ \quad \left(\overline{v}\dfrac{\partial \overline{w}}{\partial y}+\overline{v}\dfrac{\partial w^*}{\partial y}+v^*\dfrac{\partial \overline{w}}{\partial y}+v^*\dfrac{\partial w^*}{\partial y}\right)+ \\ \quad \left(\overline{w}\dfrac{\partial \overline{w}}{\partial z}+\overline{w}\dfrac{\partial w^*}{\partial z}+w^*\dfrac{\partial \overline{w}}{\partial z}+w^*\dfrac{\partial w^*}{\partial z}\right) \\ \quad =-\dfrac{1}{\rho}\dfrac{\partial \overline{p}}{\partial x}-\dfrac{1}{\rho}\dfrac{\partial p^*}{\partial x}-g+A_{\mathrm{H}}\left(\dfrac{\partial^2 \overline{w}}{\partial x^2}+\dfrac{\partial^2 \overline{w}}{\partial y^2}\right)+ \\ \quad A_{\mathrm{V}}\dfrac{\partial^2 \overline{w}}{\partial z^2}+A_{\mathrm{H}}\left(\dfrac{\partial^2 w^*}{\partial x^2}+\dfrac{\partial^2 w^*}{\partial y^2}\right)+A_{\mathrm{V}}\dfrac{\partial^2 w^*}{\partial z^2}. \end{cases} \tag{4}$$

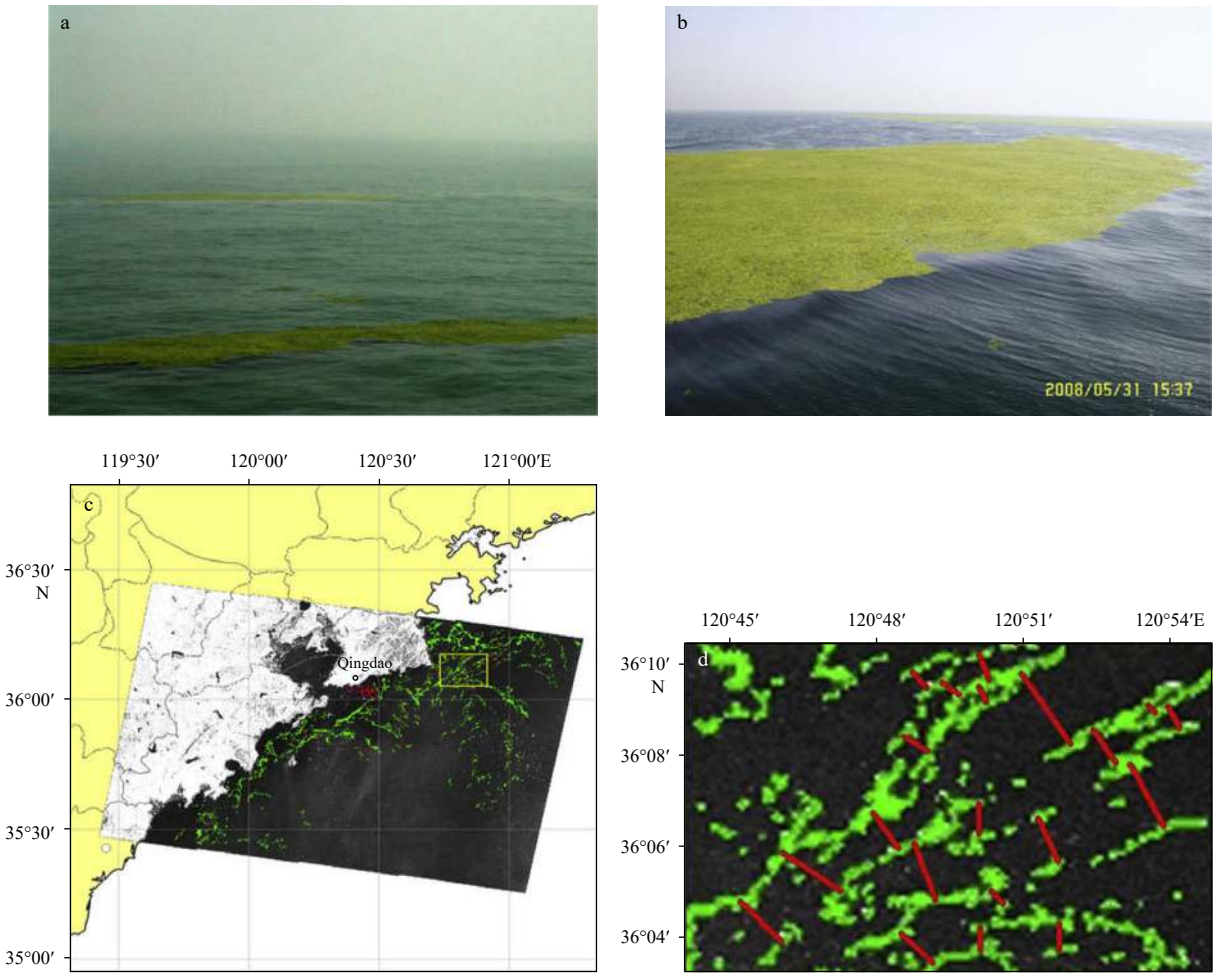

Fig. 1. The banded structure of the drifting macroalgae on the sea surface. a. A photograph from a vessel on 6 July 2008 at (36°00′18″N, 120°29′48″E), the two bands of macroalgae are about 400 m apart; b. a photograph taken from an aircraft at 15:37 on 31 May 2008 off Qingdao; c. SAR images of the macroalgae obtained from COSMO-2 on 13 July 2008; and d. subfigure magnified from the box in c (after Qiao et al. (2009)).

Fig. 2. Cloud street in West Australia (from http://www.360doc.com/content/10/1111/15/3566297_68487378.shtml).

Because $\overline{u}^* = \overline{v}^* = \overline{w}^* = \overline{p}^* = 0$, and $\overline{w} \ll \overline{u}, \overline{v}$, after subtracting the mean equations from the full equations, and omit the second order small terms, we can derive the perturbation equations:

$$\begin{cases} \dfrac{\partial u^*}{\partial x} + \dfrac{\partial v^*}{\partial y} + \dfrac{\partial w^*}{\partial z} = 0, \\ \dfrac{\partial u^*}{\partial t} + \overline{u}\dfrac{\partial u^*}{\partial x} + u^*\dfrac{\partial \overline{u}}{\partial x} + \overline{v}\dfrac{\partial u^*}{\partial y} + v^*\dfrac{\partial \overline{u}}{\partial y} + w^*\dfrac{\partial \overline{u}}{\partial z} - \\ \quad fv^* = -\dfrac{1}{\rho}\dfrac{\partial p^*}{\partial x} + A_{\mathrm{H}}\left(\dfrac{\partial^2 u^*}{\partial x^2} + \dfrac{\partial^2 u^*}{\partial y^2}\right) + A_{\mathrm{V}}\dfrac{\partial^2 u^*}{\partial z^2}, \\ \dfrac{\partial v^*}{\partial t} + \overline{u}\dfrac{\partial v^*}{\partial x} + u^*\dfrac{\partial \overline{v}}{\partial x} + \overline{v}\dfrac{\partial v^*}{\partial y} + v^*\dfrac{\partial \overline{v}}{\partial y} + w^*\dfrac{\partial \overline{v}}{\partial z} + \\ \quad fu^* = -\dfrac{1}{\rho}\dfrac{\partial p^*}{\partial y} + A_{\mathrm{H}}\left(\dfrac{\partial^2 v^*}{\partial x^2} + \dfrac{\partial^2 v^*}{\partial y^2}\right) + A_{\mathrm{V}}\dfrac{\partial^2 v^*}{\partial z^2}, \\ \dfrac{\partial w^*}{\partial t} + \overline{u}\dfrac{\partial w^*}{\partial x} + \overline{v}\dfrac{\partial w^*}{\partial y} = -\dfrac{1}{\rho}\dfrac{\partial p^*}{\partial z} + \\ \quad A_{\mathrm{H}}\left(\dfrac{\partial^2 w^*}{\partial x^2} + \dfrac{\partial^2 w^*}{\partial y^2}\right) + A_{\mathrm{V}}\dfrac{\partial^2 w^*}{\partial z^2}. \end{cases} \tag{5}$$

The boundary conditions for the perturbation equations are

$$\begin{cases} u^* = v^* = w^* = 0, \quad z = -H; \\ \dfrac{\partial u^*}{\partial z} = \dfrac{\partial v^*}{\partial z}, \quad w^* = 0, \quad z = 0. \end{cases} \tag{6}$$

2.2 *Mean flow*

Since the macroalgae mainly gathered in the region of (35.0°–37.0°N, 119.2°–122.0°E) in the Yellow Sea, we collected *in-situ* ocean current data from one station located at (36°02′N, 121°05′E). The position of the observation site is shown in Fig. 3. The data were obtained with an acoustic Doppler current profiler. We processed the data as follows: (1) used a 7-point smoothing filter, any velocity signal with period less than 1 h was removed; (2) the one-hour interval data were selected; and (3) low-pass filtering was performed using the Lanczos window cosine squared filter, and the mean flow removing the main tidal current was obtained. In fact, this mean flow is the wind driven Ekman drift current.

Figure 4 shows the obtained one-hour interval current data from 14:00 to 19:00 on 16 July. There is no significant difference in the velocity structure, so we just show the three-dimensional vector diagram of the velocity at 14:00 in Fig. 5.

2.3 *The secondary circulation*

2.3.1 *The motion equations*

For many cases of the banded structure, there is usually an angle θ between the band axis and the surface mean flow (Dong, 1997; Noh et al., 2004). As we are concerned with the secondary circulation, we can rotate the horizontal coordinate axis counterclockwise with the angle of θ for the convenience of the following analysis and discussion. The direction of the new coordinate after rotation becomes the same as that of the rotation axis of the secondary circulation. Thus, in the new coordinate, the secondary

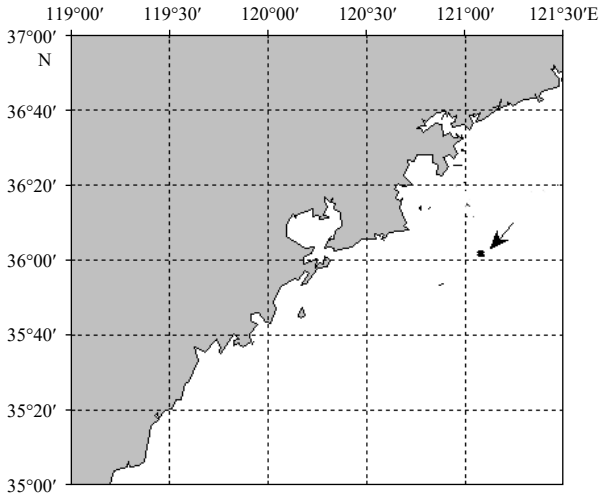

Fig. 3. Location (36°02'N, 121°05'E) of the observed velocity profile. Depth is roughly 30 m.

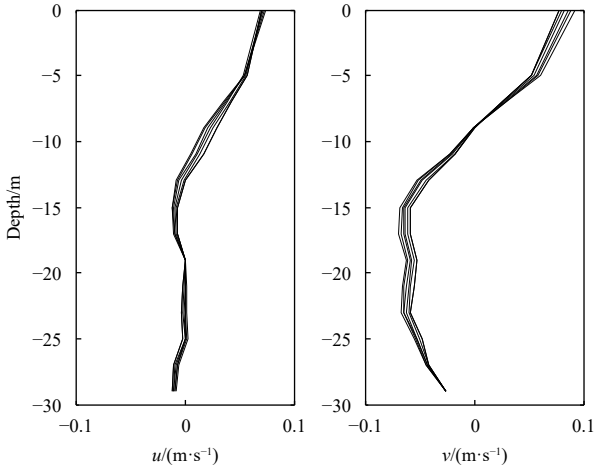

Fig. 4. The obtained 1-h interval mean ocean current of u and v from 14:00 to 19:00. The current is Emkan drift current.

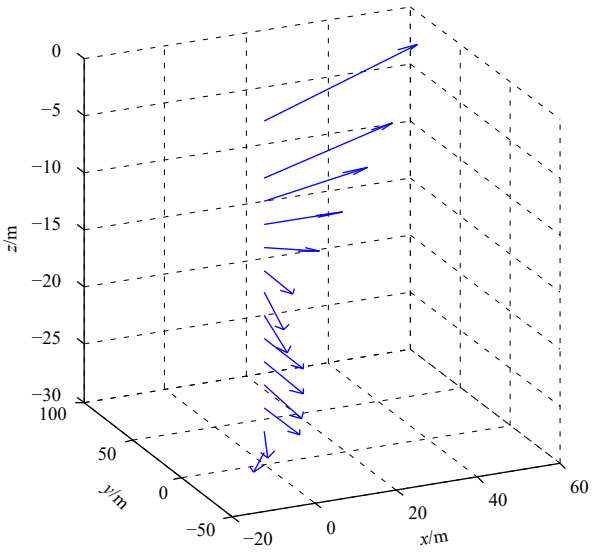

Fig. 5. Three-dimensional vector diagram of the obtained mean flow at 14:00.

circulation is a two-dimensional flow. Meanwhile, D, u_0 and $D/u_0$are used as length, velocity, and time scales, respectively. D is the Ekman depth, and u_0 is the surface velocity. We define new variables as follows:

$$\begin{cases} x' = (x\cos\theta + y\sin\theta)/D, \\ y' = (-x\sin\theta + y\cos\theta)/D, \\ z' = z/D, \\ u' = (u^*\cos\theta + v^*\sin\theta)/u_0, \\ v' = (-u^*\sin\theta + v^*\cos\theta)/u_0, \\ w' = w^*/u_0, \\ u = (\bar{u}\cos\theta + \bar{v}\sin\theta)/u_0, \\ v = (-\bar{u}\sin\theta + \bar{v}\cos\theta)/u_0. \end{cases} \tag{7}$$

Since the secondary circulation is a two-dimensional flow in the new coordination system, each variable of the disturbance is uniform in the direction x, so the derivative along the direction x is zero. We can obtain the non-dimensional perturbation equations as follows:

$$\frac{\partial v'}{\partial y'} + \frac{\partial w'}{\partial z'} = 0, \tag{8-1}$$

$$Re\left(\frac{\partial u'}{\partial t} + v\frac{\partial u'}{\partial y'} + w'\frac{\partial u}{\partial z'}\right) - 2v' = \gamma\frac{\partial^2 u'}{\partial y'^2} + \frac{\partial^2 u'}{\partial z'^2}, \tag{8-2}$$

$$Re\left(\frac{\partial v'}{\partial t} + v\frac{\partial v'}{\partial y'} + w'\frac{\partial v}{\partial z'} + \frac{\partial p'}{\partial y}\right) + 2u' = \gamma\frac{\partial^2 v'}{\partial y'^2} + \frac{\partial^2 v'}{\partial z'^2}, \tag{8-3}$$

$$Re\left(\frac{\partial w'}{\partial t} + v\frac{\partial w'}{\partial y'} + \frac{\partial p'}{\partial z}\right) = \gamma\frac{\partial^2 w'}{\partial y'^2} + \frac{\partial^2 w'}{\partial z'^2}, \tag{8-4}$$

where $Re = u_0 D/A_V, \gamma = A_H/A_V$, and u', v', w', p', u, v are non-dimensional variables in the new coordinate system, with the prime symbol indicating the perturbation.

The two-dimensional continuity equation in Eq. (8-1) allows the introduction of a stream function ψ', $v' = -\frac{\partial \psi'}{\partial z'}$, and $w' = \frac{\partial \psi'}{\partial y'}$.

By cross differentiation of Eqs (8–3) and (8–4), a new equation can be obtained:

$$Re\left(\frac{\partial}{\partial t}\nabla^2\psi' + v\frac{\partial}{\partial y'}\nabla^2\psi' - \frac{\partial^2\psi'}{\partial y'\partial z'}\frac{\partial v}{\partial z'} - \frac{\partial\psi'}{\partial y'}\frac{\partial^2 v}{\partial z'^2}\right) - 2\frac{\partial u'}{\partial z'}$$
$$= \beta\frac{\partial^4\psi'}{\partial y'^4} + (1+\gamma)\frac{\partial^4\psi'}{\partial y'^2\partial z'^2} + \frac{\partial^4\psi'}{\partial z'^4}. \tag{9}$$

2.3.2 *Stability analysis*

The purpose of the stability analysis was to investigate the evolution of the solution to Eqs (8-2) and (9) over time. When $t\to\infty$, if all the possible solutions are close to zero, the original flow would be stable. If there is a single solution that dissatisfies the condition, then the original flow would be unstable.

Because the coefficients of Eqs (8-2) and (9) are related to z only, we assume the form of the disturbance to be

$$\begin{cases} u' = \hat{u}(z)\exp[\mathrm{i}(ay - \omega t)], \\ \psi' = \hat{\psi}(z)\exp[\mathrm{i}(ay - \omega t)], \end{cases} \tag{10}$$

where $\hat{u}$ is a complex amplitude, and a is the wave number. We take the wave number a as a real number because we focus on the evolution of the disturbance in time, and $\omega = \omega_r + \mathrm{i}\omega_\mathrm{i}$ is a complex number, where ω_i is the imaginary part of ω. After substituting Eq. (10) into Eqs (8-2) and (9), we get the characteristic equations as follows:

$$\begin{cases} \frac{\mathrm{d}^2\hat{u}}{\mathrm{d}z'^2} - \gamma a^2\hat{u} - \mathrm{i}aRe\left[(v-\omega/a)\hat{u} + \frac{\mathrm{d}u}{\mathrm{d}z'}\hat{\psi}\right] - 2\frac{\mathrm{d}\hat{\psi}}{\mathrm{d}z'} = 0, \\ \frac{\mathrm{d}^4\hat{\psi}}{\mathrm{d}z'^4} - (1+\gamma)\,a^2\frac{\mathrm{d}^2\hat{\psi}}{\mathrm{d}z'^2} + \beta a^4\hat{\psi} - \mathrm{i}aRe\Big[(v-\omega/a)\times \\ \qquad\left(\frac{\mathrm{d}^2\hat{\psi}}{\mathrm{d}z'^2} - a^2\hat{\psi}\right) - \frac{\mathrm{d}^2 v}{\mathrm{d}z'^2}\hat{\psi}\Big] + 2\frac{\mathrm{d}\hat{u}}{\mathrm{d}z'} = 0. \end{cases} \tag{11}$$

The boundary conditions are

$$\begin{cases} \hat{\psi} = \frac{\mathrm{d}\hat{\psi}}{\mathrm{d}z'} = \hat{u} = 0, \quad z' \to -H/D; \\ \hat{\psi} = \frac{\mathrm{d}^2\hat{\psi}}{\mathrm{d}z'^2} = \frac{\mathrm{d}\hat{u}}{\mathrm{d}z'} = 0, \quad z' = 0. \end{cases} \tag{12}$$

Because Eq. (11) and the boundary condition Eq. (12) are homogeneous, if it has nonzero solutions, the parameters Re, a, θ, ω, γ must satisfy some functional relationship such as:

$$F(Re, a, \theta, \omega, \gamma) = 0. \tag{13}$$

Equation (13) can be called a characteristic relation. From this equation, we get the complex eigenvalue ω when Re, a, θ, γ are given. As the analytical solutions for the above-mentioned characteristic values are difficult, so we will find their numerical solutions.

3 Analysis of numerical results

To get the values of the non-dimensional scales we used above, we refer to the empirical relationship (shown below) between the surface velocity u_0, friction depth $\widehat{D}$, and the wind speed W, which were obtained by Ekman through analyzing many observations (Feng et al., 1999).

$$\begin{cases} u_0/W = 0.012\ 7/\sqrt{\sin|\varphi|}, \\ \widehat{D} = 4.3W/(\sqrt{\sin|\varphi|}), \end{cases} \tag{14}$$

where the unit of W is m/s. And there is a coefficient π between the friction depth $\widehat{D}$ and the Ekman depth D. That is,

$$D = \widehat{D}/\pi = 4.3W/(\pi\sqrt{\sin|\varphi|}). \tag{15}$$

Thus, if we have data for latitude φ and wind speed W, we can obtain the values of D and u_0. For the wind speed W, we used the QSCAT/NCEP blended wind field data. Because the macroalgae

mainly gathered in the region of (35.0°–37.0°N, 119.2°–122.0°E) in the Yellow Sea, we used wind data from the point (36.0°N, 120.5°E) as representative. The observed wind speed in June and July 2008 is shown in Fig. 6. The mean wind speed was 6.8 m/s during that time, and we set W=6.8 m/s, so:

$$\begin{cases} u_0 \approx 0.11 \text{ m/s}, \\ D \approx 12.1 \text{ m}. \end{cases} \tag{16}$$

The value of A_H, A_V is difficult to determine, we take it to be $A_v = 5 \times 10^{-3}$ m^2/s (Large, 1994), as vertical mixing dominated by non-breaking surface wave is very strong in the upper ocean (Qiao et al., 2004, 2016), to take this A_V value is reasonable. Then we get $Re \approx 200$. We do not give the exact value for A_H, but it can be calculated from A_V and γ.

In the following section, we conduct a series of numerical experiments using different Reynolds numbers, wave numbers, and declination angles. Their values are shown in Table 1.

In Fig. 7, we show how the imaginary part ω_i of the complex eigenvalue ω behaves as the Reynolds number changes. According to the stability theory, when $\omega_i > 0$, the modulus of the perturbation increases, and the original laminar flow would be unstable. Thus, when $\omega_i < 0$, the modulus of the perturbation would decrease and the original laminar flow would be stable, and when $\omega_i = 0$, the modulus of the perturbation would be unchanged, which is called the neutral condition. As shown in Fig. 7, the eigenvalue distributions have different characters with the parameters changing. They are not significantly different because the Re data we chose are very close. With increasing Re, the range of the unstable state grows, the wave number of the most unstable state increases gradually, and declination also becomes larger; however, the general range of the declination angle is between 5° and 20°. Meanwhile, the maximum value of ω_i becomes smaller with increasing Re. Yet the maximum of the imaginary part of the complex eigenvalue is mostly above 0.01. This number represents the growth speed of the perturbation, that is, the time which perturbation growing needs is $T = 1/\omega_i < 1/0.01 = 100$. This is non-dimensional time. If we use the dimensionless criterion shown above, $T = D/u_0$, we can get dimensional time as below: $t = 100T = 100D/u_0 \approx 100 \times 12.1$ m/(0.11 m/s) = 11 000 s ≈3 h.

Then, we check the spatial scale of secondary circulation. Figure 7 shows that the wave number of the unstable state has a large range, which is concentrated between 0.5 and 1.0. Therefore, we can get the wavelength $\lambda = (2\pi/a) \cdot D$. Here, we can use D = 12.1 m for consistency with the previous part of the paper, and we find that the wavelength is in the range of 75–150 m.

Meanwhile, if we take Re = 200 as an example, we show the max value of the imaginary part of the complex eigenvalue with varying wave number (Fig. 8). It is clear from the first panel of the figure that when the wave number value equals 0.05 or higher, the imaginary part of the complex eigenvalue becomes positive. The unstable state appears; the corresponding declination angle is about 5°. From the other panels, it is clear that with increasing wave number, the unstable state always exists until wave number value becomes 1.5, and the corresponding declination angle also increases gradually. Figure 9 shows the maximum value of the imaginary part of the complex eigenvalue with varying decli-

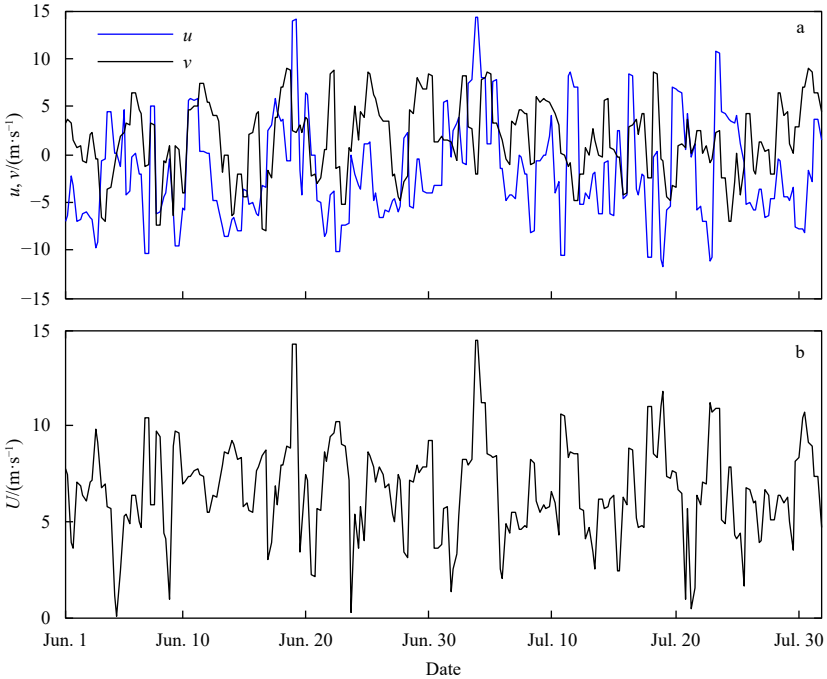

Fig. 6. The observed wind components of u and v (a), and wind speed U (b) in June and July of 2008.

Table 1. Values used in numerical experiments

Parameters	Values
Reynolds number (Re)	100, 150, 200, 250, 300, 350, 400, 450
A_H/A_V (γ)	1:10:1 000
Wave number (a)	0.2, 0.4, 0.6, 0.8, 1.0, 1.2, 1.4, 1.6, 1.8, 2.0
Declination angle (θ)/(°)	–50, –45, –40, –35, –30, –25, –20, –15, –10, –5, 0, 5, 10, 15, 20, 25, 30, 35, 40, 45, 50

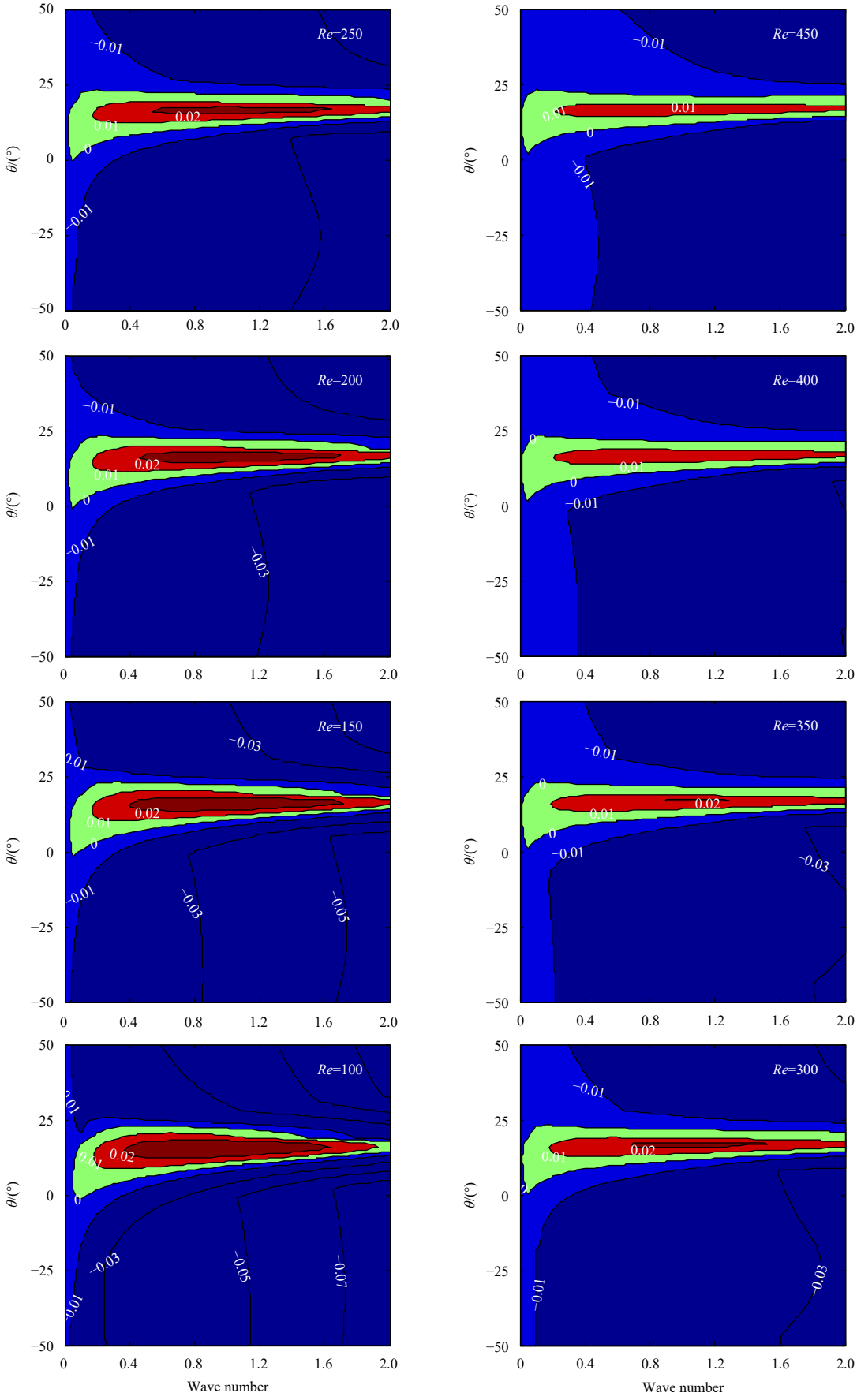

Fig. 7. Distribution of the imaginary part of the complex eigenvalue with varying Reynolds number ($\gamma = 1$).

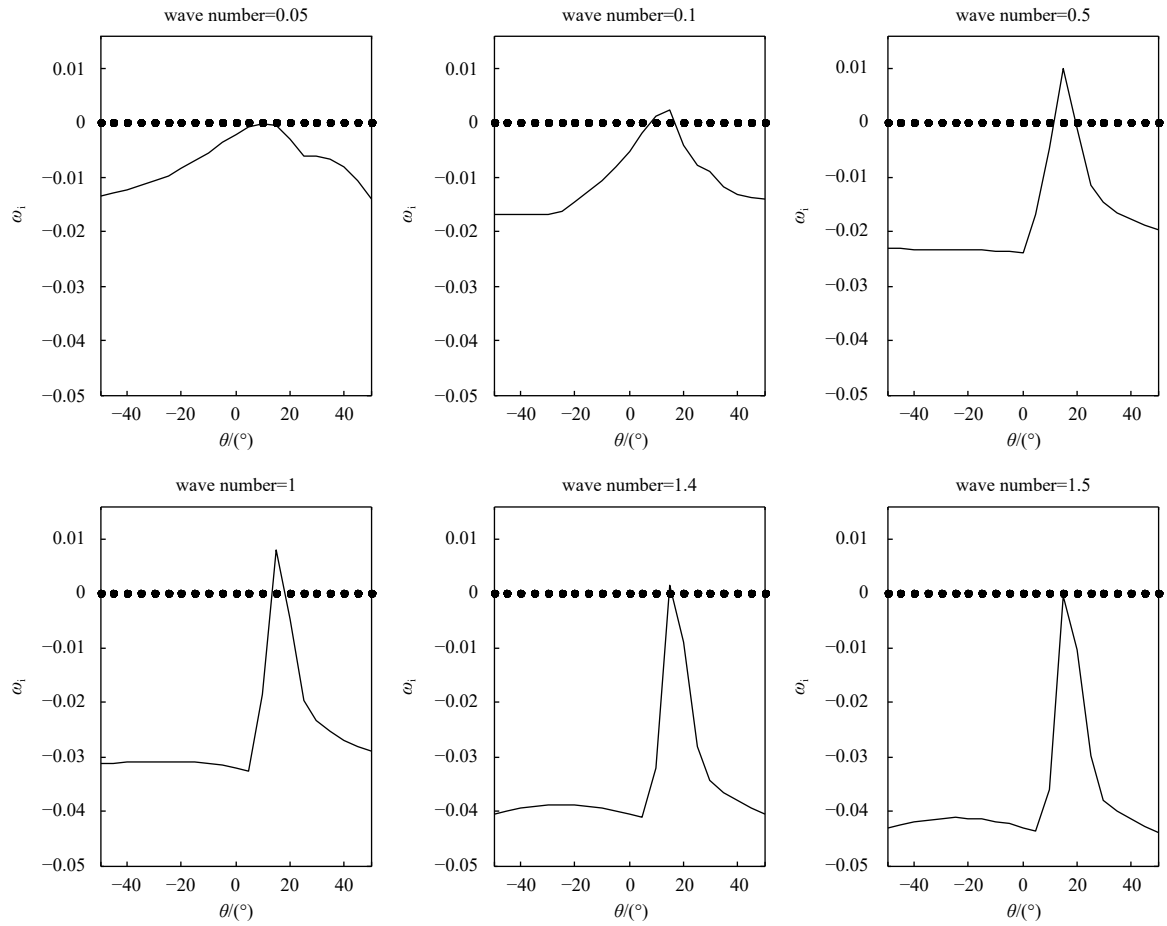

Fig. 8. The imaginary part of the complex eigenvalue with varying wave number.

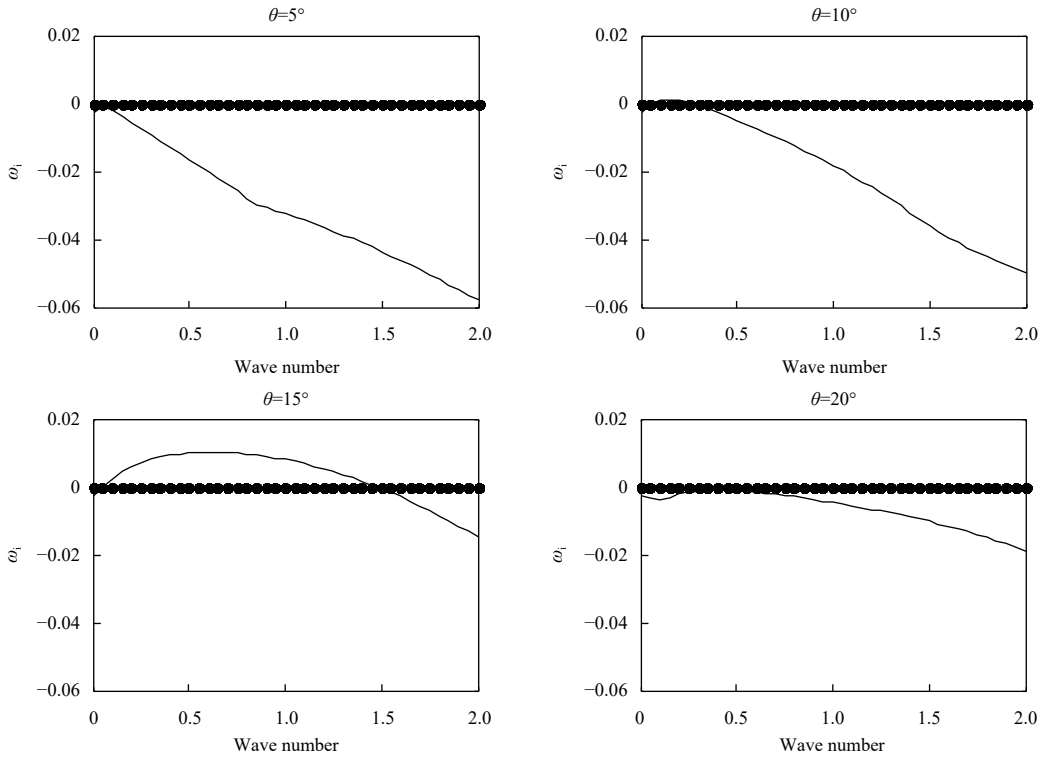

Fig. 9. The imaginary part of complex eigenvalue with varying declination angle.

nation angle. When the declination angle equals 5° or higher, the imaginary part of the complex eigenvalue becomes positive, with the increase of the declination angle unstable state always existing until the wave number value equals 20°.

To consider the influence of the horizontal and vertical eddy viscosity coefficients A_H, A_V, the relationship between γ and the maximum value of the imaginary part of the complex eigenvalue ω_i and its corresponding wave number and angle are shown in Fig. 10. We just show two different *Re* values (*Re* = 200, 500). No matter how much we define the value of *Re*, the corresponding wave number usually decreases with increasing γ. In other words, the spatial scale of the secondary circulation induced from the instability will magnify when γ increases. We can also see that the corresponding angle decreases with increasing γ, but that the angle is always positive. This means that the axis of the secondary circulation is always on the left side of the mean flow.

To go into further detail, when $\gamma = 50$, we show how the imaginary part ω_i of the complex eigenvalue ω behaves as the Reynolds number changes (Fig. 11). It is clear that with increasing Reynolds number: the range of the unstable state becomes larger, the wave number of the most unstable state increases gradually, and declination also becomes larger, but the general range of the declination angle is between 5° and 15°. In addition, we can see that the wave number of the unstable state becomes less than 0.1 (Fig. 11). The wavelength is about 800 m.

To detect the character of the secondary circulation more clearly, we chose one unstable state for simulation. The choosed parameters are as follows: *Re* = 200, wave number (a) = 0.1, angle (θ) = 10°, and γ = 50.

The stream function of the secondary circulation are shown in Fig. 12. The distance between two convergence fields is about 30 times of the ocean depth, so it is about 1 km. Therefore, it matches the observed spatial scale of the surface drifting macroalgae distribution, suggesting that secondary circulation related to the instability of the wind driven Ekman drift current is responsible for the banded structure.

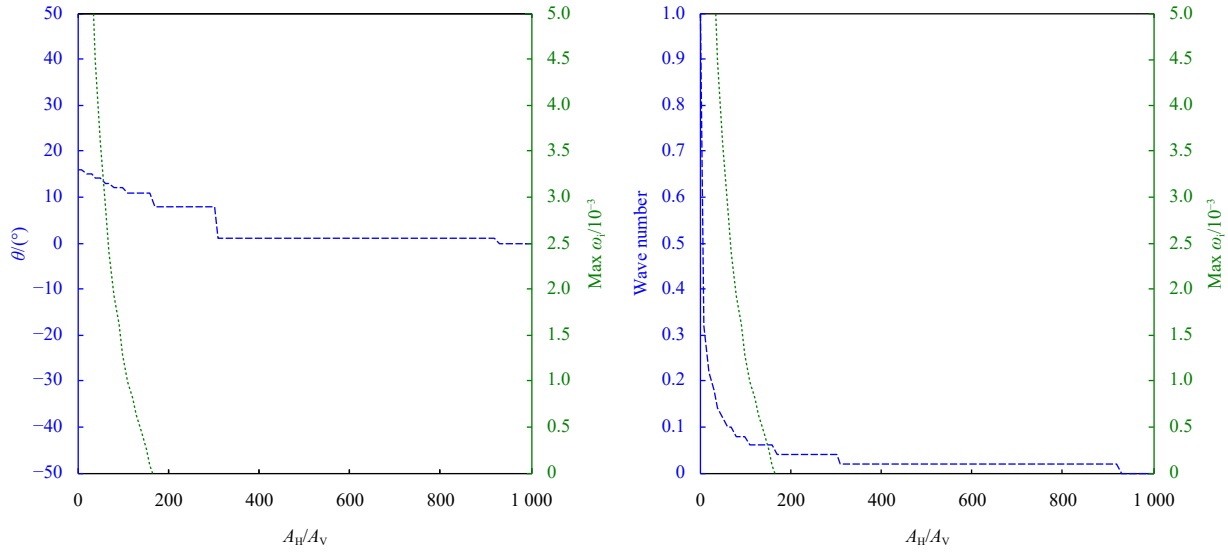

a. *Re*=200

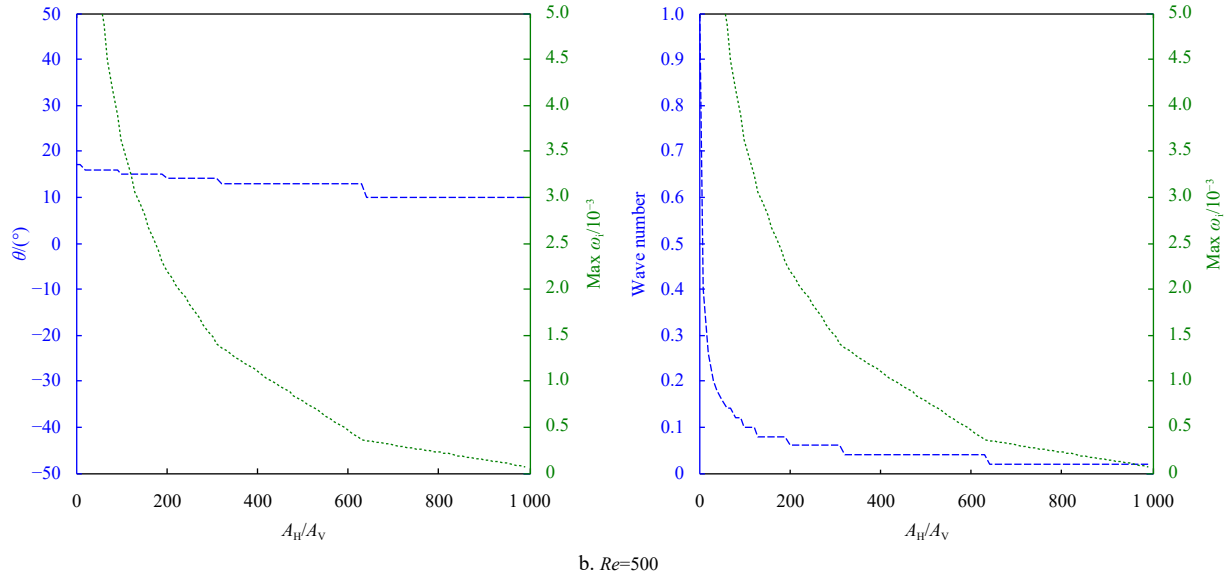

b. *Re*=500

Fig. 10. Influence of the ratio between the horizontal and vertical eddy viscosity coefficients.

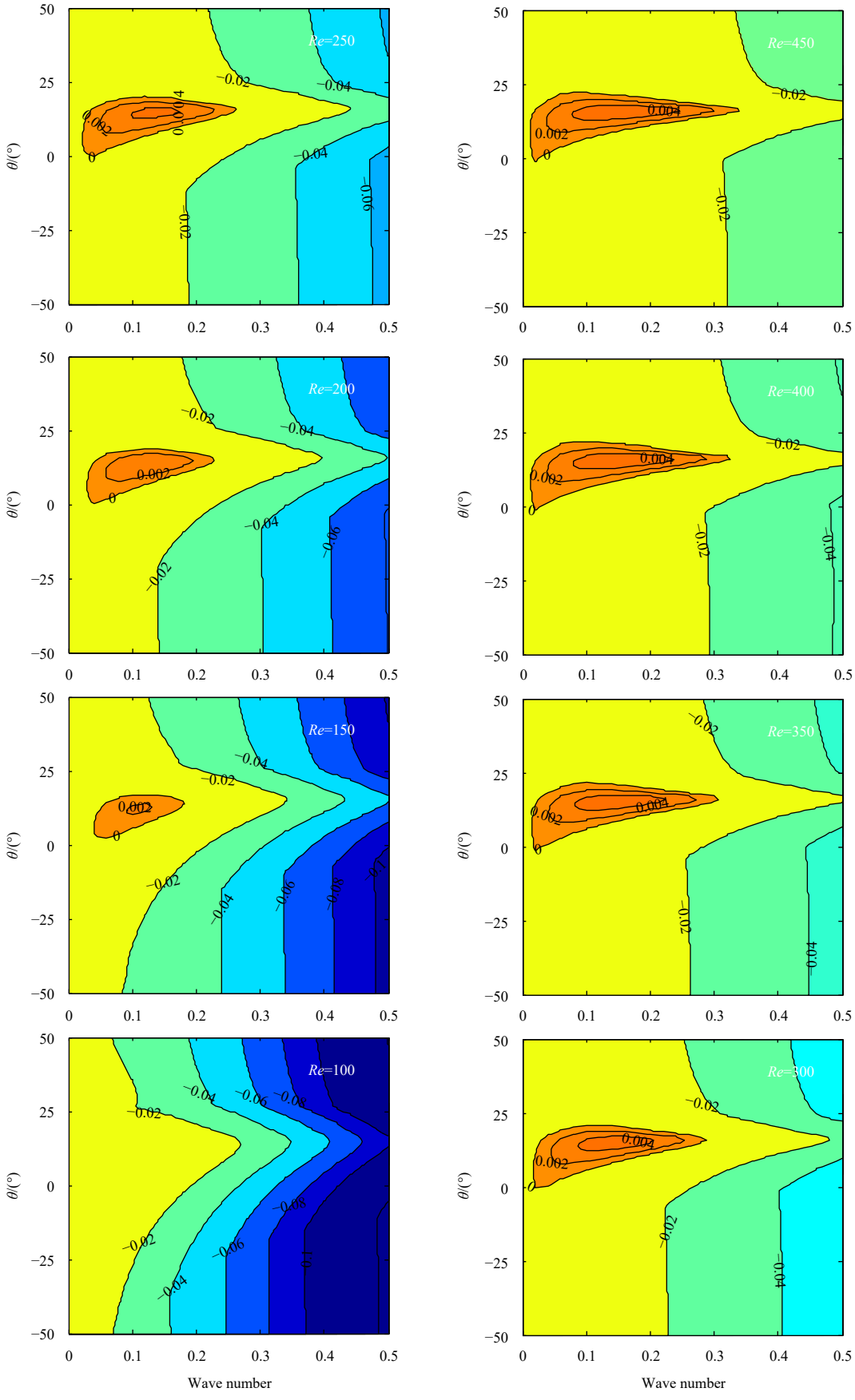

Fig. 11. Distribution of imaginary part of complex eigenvalue with varying Reynolds number ($\gamma = 50$).

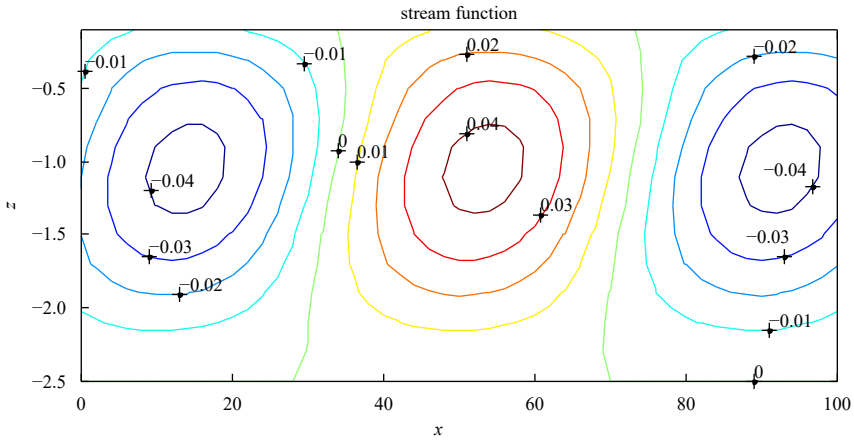

Fig. 12. The simulated stream function.

4 Discussion and conclusions

The banded structure observed in the macroalgae bloom period in the Yellow Sea should indicate a new dynamic process in the upper ocean. From instability analysis, we found that the secondary circulation related to the stability of the wind driven Ekman drift current is responsible for the banded structure. The places where the banded structure occurred are convergence zones caused by a pair of secondary circulations, so any floating materials such as macroalgea bloom, ocean debris, oil spills will be accumulated in these convergent zones. In fact, both the oil pollution in the Gulf of Mexico in 2010 and the *Sanchi* oil spill in 2018 showed similar banded structure, which is incorrectly attribute to the Langmuir circulation. By the way, the divergent zone with the same spatial scale will have higher biological productivity. So, this new circulation could have a great influence on the ocean environment and marine ecosystem. For instance, it could have practical applications for the prevention and control of marine disasters, such as algal blooms, ocean debris and oil spills. More importantly, this is a new channel between the upper ocean and subsurface layer to exchange energy, materials, gas, etc. and this secondary circulation can be applied in the development of ocean and climate models. This new discovered secondary circulation, on which the corresponding author of this paper has paid high attention since 2008, in the ocean is a subject of high research value, which can enrich our knowledge on the ocean dynamics in the surface boundary layer.

By analyzing the featured distribution of the growth rates, we found that the spatial scale of the secondary circulation fits well with the observation by Qiao et al. (2009). This paper gives a dynamical explanation for the banded structure of the drifting macroalgae through traditional stability analysis. This result is not only an interesting phenomenon, but also may provide a new mechanism of vertical mixing in the upper ocean which is important for ocean and climate model development. The detailed research on the secondary circulation may be via observations; however, it is difficult to undertake such kind of direct measurement, which of course brings obstacles and difficulties for a designed scientific experiment. The macroalgea bloom provide us an excellent opportunity to reveal the mechanism of the secondary circulation.

References

Brown R A. 1970. A secondary flow model for the planetary boundary layer. Journal of the Atmospheric Sciences, 27(5): 742–757, doi: 10.1175/1520-0469(1970)027<0742:ASFMFT>2.0.CO;2

Dong Changming. 1997. Formation mechanism of modern tidal current sand ridges (in Chinese) [dissertation]. Qingdao: Institute of Oceanography, Chinese Academy of Sciences

Feng Shizuo, Li Fengqi, Li Shaojing. 1999. An Introduction to Marine Science (in Chinese). Beijing: Higher Education Press, 161

Langmuir I. 1938. Surface motion of water induced by wind. Science, 87(2250): 119–123, doi: 10.1126/science.87.2250.119

Large W G, McWilliams J C, Doney S C. 1994. Oceanic vertical mixing: a review and a model with a nonlocal boundary layer parameterization. Reviews of Geophysics, 32: 363–403, doi: 10.1029/94RG01872

Leibovich S. 1983. The form and dynamics of Langmuir circulation. Annual Review of Fluid Mechanics, 15: 391–427, doi: 10.1146/annurev.fl.15.010183.002135

Lilly D K. 1966. On the instability of Ekman boundary flow. Journal of the Atmospheric Sciences, 23(5): 481–494, doi: 10.1175/1520-0469(1966)023<0481:OTIOEB>2.0.CO;2

Noh Y, Min H S, Raasch S. 2004. Large eddy simulation of the ocean mixed layer: The effects of wave breaking and Langmuir circulation. Journal of Physical Oceanography, 34(4): 720–735, doi: 10.1175/1520-0485(2004)034<0720:LESOTO>2.0.CO;2

Pollard R T. 1977. Observations and theories of Langmuir circulations and their role in near surface mixing. In: Angel M, ed. A Voyage of Discovery: George Deacon 70th Anniversary Volume. Oxford: Pergamon, 235–251

Qiao Fangli, Dai Dejun, Simpson J, et al. 2009. Banded structure of drifting macroalgae. Marine Pollution Bulletin, 58(12): 1792–1795, doi: 10.1016/j.marpolbul.2009.08.006

Qiao Fangli, Yuan Yeli, Deng Jia, et al. 2016. Wave turbulence interaction induced vertical mixing and its effects in ocean and climate models. Philosophical Transactions of the Royal Society of London Series A—Mathematical, Physical and Engineering Sciences, 374(2065): 20150201, doi: 10.1098/rsta.2015.0201

Qiao Fangli, Yuan Yeli, Yang Yongzeng, et al. 2004. Wave-induced mixing in the upper ocean: distribution and application to a global ocean circulation model. Geophysical Research Letters, 31(11): L11303

Thorpe S A. 2004. Langmuir circulation. Annual Review of Fluid Mechanics, 36: 55–79, doi: 10.1146/annurev.fluid.36.052203.071431

Thorpe S A. 2009. Spreading of floating particles by Langmuir circulation. Marine Pollution Bulletin, 58(12): 1787–1791, doi: 10.1016/j.marpolbul.2009.07.022